ARTICLE

Halide perovskites as disposable epitaxial templates for the phase-selective synthesis of lead sulfochloride nanocrystals

Stefano Toso [1,2,8], Muhammad Imran [1,8✉], Enrico Mugnaioli [3], Anna Moliterni [4✉], Rocco Caliandro [4], Nadine J. Schrenker [5], Andrea Pianetti [6], Juliette Zito[1,7], Francesco Zaccaria[1], Ye Wu[1], Mauro Gemmi [3✉], Cinzia Giannini [4], Sergio Brovelli [6✉], Ivan Infante[1✉], Sara Bals [5✉] & Liberato Manna [1✉]

Colloidal chemistry grants access to a wealth of materials through simple and mild reactions. However, even few elements can combine in a variety of stoichiometries and structures, potentially resulting in impurities or even wrong products. Similar issues have been long addressed in organic chemistry by using reaction-directing groups, that are added to a substrate to promote a specific product and are later removed. Inspired by such approach, we demonstrate the use of $CsPbCl_3$ perovskite nanocrystals to drive the phase-selective synthesis of two yet unexplored lead sulfochlorides: $Pb_3S_2Cl_2$ and $Pb_4S_3Cl_2$. When homogeneously nucleated in solution, lead sulfochlorides form $Pb_3S_2Cl_2$ nanocrystals. Conversely, the presence of $CsPbCl_3$ triggers the formation of $Pb_4S_3Cl_2/CsPbCl_3$ epitaxial heterostructures. The phase selectivity is guaranteed by the continuity of the cationic subnetwork across the interface, a condition not met in a hypothetical $Pb_3S_2Cl_2/CsPbCl_3$ heterostructure. The perovskite domain is then etched, delivering phase-pure $Pb_4S_3Cl_2$ nanocrystals that could not be synthesized directly.

[1] Department of Nanochemistry, Istituto Italiano di Tecnologia, Via Morego 30, 16163 Genova, Italy. [2] International Doctoral Program in Science, Università Cattolica del Sacro Cuore, 25121 Brescia, Italy. [3] Electron Crystallography, Center for Materials Interfaces, Istituto Italiano di Tecnologia, Viale Rinaldo Piaggio 34, 56025 Pontedera, Italy. [4] Istituto di Cristallografia – Consiglio Nazionale delle Ricerche (IC–CNR), Via Giovanni Amendola 122/O, 70126 Bari, Italy. [5] Electron Microscopy for Materials Science (EMAT) and NANOlab Center of Excellence, University of Antwerp, Groenenborgerlaan 171, 2020 Antwerp, Belgium. [6] Dipartimento di Scienza dei Materiali, Università degli Studi di Milano-Bicocca, Via Roberto Cozzi 55, 20125 Milano, Italy. [7] Dipartimento di Chimica e Chimica Industriale, Università degli Studi di Genova, Via Dodecaneso 31, 16146 Genova, Italy. [8]These authors contributed equally: Stefano Toso, Muhammad Imran. ✉email: muhd.imran.phd@gmail.com; annagrazia.moliterni@ic.cnr.it; mauro.gemmi@iit.it; sergio.brovelli@unimib.it; ivan.infante@iit.it; sara.bals@uantwerpen.be; liberato.manna@iit.it

Since its early days[1], the research on colloidal nanocrystals (NCs) has provided access to a variety of inorganic compounds, spanning from metals and alloys[2] to oxides[3,4], phosphides[5], chalcogenides[6–11], halides[12,13], and more. Nowadays, NCs are exploited in many different fields, as NCs-based products are steadily finding their way to commercial applications[14–18]. A colloidal approach to the synthesis of inorganic materials offers several advantages over more traditional solid-state chemistry techniques, such as milder reaction conditions, ease of tunability deriving from a wider choice of precursors, better processability of the products, and straightforward access to nanostructured materials. However, both this flexibility and the push toward materials combining a higher number of elements come at the cost of increased complexity. One example is the field of colloidal semiconductors, where lead-based NCs are among the most explored compounds due to the appealing optoelectronic properties demonstrated by lead halide perovskites in the UV-VIS and by lead chalcogenides in the IR spectral ranges[6,7,12,13,19]. There, the combination of as little as four elements (Cs, Pb, X and E, where X = F, Cl, Br or I, and E = S, Se or Te) can yield NCs of a variety of phases: the binaries CsX, PbX_2, and PbE[6,7,20–22], the well-known cesium lead halides (Cs_4PbX_6, $CsPbX_3$, and $CsPb_2X_5$)[12,19,23,24], and the still little explored lead chalcohalides ($Pb_4S_3Br_2$ and $Pb_4S_3I_2$)[25,26]. All these compounds are often obtained under similar reaction conditions, and can therefore compete during the synthesis, requiring a careful tuning of the synthetic protocols to achieve an impurity-free synthesis of the desired product.

This condition is not dissimilar from that of many organic chemistry reactions, where two molecules can react following different pathways and resulting in different products. Similar issues are often addressed by exploiting reaction-directing groups, that are moieties which are attached to one of the reagents in order to direct the reaction pathway toward the desired product, and are removed at a later stage[27]. This requires a multi-step rational design of the synthetic procedure, that is common for organic chemistry but is missing in the colloidal synthesis of NCs, as most procedures consist of a one-step reaction.

In this work, we exploit the formation of epitaxial heterostructures as a reaction-directing step for the phase-selective synthesis of colloidal NCs, and we take advantage of this approach to further expand the family of lead chalcohalides. These materials share the general formula $Pb_aE_bX_c$, and only four stable compositions are known in bulk ($PbTeF_6$, $Pb_7S_2Br_{10}$, $Pb_5S_2I_6$, Pb_4SeBr_6)[28,29], together with two recently reported high-pressure metastable phases ($Pb_4S_3I_2$, $Pb_3Se_2Br_2$)[30,31]. Our group pioneered the investigation of lead chalcohalides at the nanoscale, discovering two additional compounds ($Pb_4S_3Br_2$ and a yet not identified Pb-S-Cl phase) in the form of NCs[25]. More recently, we found that $Pb_4S_3Br_2$ can match epitaxially the $CsPbX_3$ perovskite to form colloidal heterostructures, thus demonstrating a remarkable synthetic and structural compatibility[26]. Here we focus our attention on the lead sulfochlorides, demonstrating that the yet unknown Pb-S-Cl phase obtained through direct synthesis is $Pb_3S_2Cl_2$, whose structure, here identified as monoclinic, is a distorted version of the cubic $Pb_3Se_2Br_2$ prototype (Fig. 1, left reaction route)[31]. Conversely, the introduction of $CsPbCl_3$ nanoclusters in the reaction medium, under comparable reaction conditions, produces $Pb_4S_3Cl_2/CsPbCl_3$ heterostructures while suppressing the formation of $Pb_3S_2Cl_2$. Once the heterostructures are formed, the perovskite domain can be etched by exploiting the solubility of $CsPbCl_3$ in polar solvents, while leaving the $Pb_4S_3Cl_2$ domains intact. Hence, the use of $CsPbCl_3$ as a disposable template yields colloidally stable $Pb_4S_3Cl_2$ NCs that could not be obtained by direct synthesis due to the competitive nucleation of $Pb_3S_2Cl_2$ (Fig. 1, top-right reaction route).

The reason why $CsPbCl_3$ induces such phase selectivity lies in the fact that the structures of $Pb_3S_2Cl_2$ and $Pb_4S_3Cl_2$ are remarkably different[25,30], to the point that only $Pb_4S_3Cl_2$ can match epitaxially with the $CsPbCl_3$ perovskite. Indeed, $Pb_4S_3Cl_2$ meets two strict structural constraints: i) the presence of a perovskite-like atomic plane[26], and ii) the continuity of the cationic subnetwork across the chalcohalide/perovskite interface[32]. Such conditions are not met for $Pb_3S_2Cl_2$, whose homogeneous nucleation is, therefore, less favorable than the heterogeneous nucleation of $Pb_4S_3Cl_2$ templated by the $CsPbCl_3$ perovskite.

Overall, our method effectively combines the concept of sacrificial substrates, such as the alkali halide single crystals used for the large-area synthesis of films and ultrathin materials[33–36], with the phase-selection capabilities ensured by the epitaxial templating, all in the liquid phase.

Results

Structure solution of $Pb_3S_2Cl_2$ NCs. We start by discussing the synthesis and structure solution of lead sulfochloride NCs prepared by homogenous nucleation, that is, in the absence of halide perovskites. We recently reported the synthesis of the same NCs by a different procedure[25], but in our previous work the small size of the particles and the heavy PbS contamination prevented us from determining the composition and crystal structure, which had therefore remained unknown to date. To solve the structure in the present work, we prepared large-size NCs via a two-step procedure, consisting of nucleation and seeded growth (Fig. 2a, b, see Supplementary Discussion, section 1 for details).

The synthesis yielded particles with a diameter of 29.5 ± 2.0 nm, as estimated by Transmission Electron Microscopy (TEM). Beyond this size the NCs became insoluble in the reaction medium, and the accretion process halted. The composition measured by SEM-EDX was Pb:S:Cl = 3.2:1.8:2.0, which is
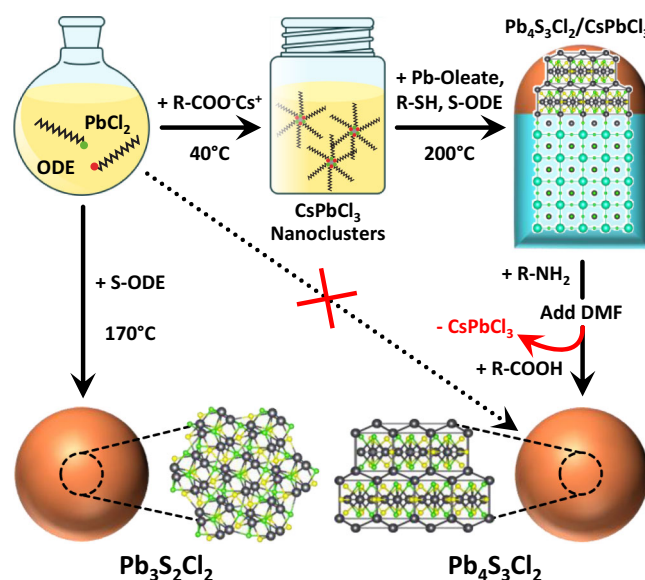

Fig. 1 Phase-selective templated synthesis of lead sulfochloride NCs. A solution of $PbCl_2$ reacts with sulfur dissolved in 1-octadecene (S-ODE) to form $Pb_3S_2Cl_2$ NCs. When reacted with Cs-oleate (R-COO⁻Cs⁺) it produces instead $CsPbCl_3$ nanoclusters, that can be further reacted with Pb-oleate, S-ODE, and an alkyl thiol (R-SH) to form $Pb_4S_3Cl_2/CsPbCl_3$ heterostructures. The $CsPbCl_3$ domain can be then selectively etched by the sequential addition of oleylamine (R-NH₂), dimethyl formamide (DMF), and oleic acid (R-COOH), yielding colloidally stable $Pb_4S_3Cl_2$ NCs that could not be obtained by direct synthesis. Atoms color code: Cs = cyan; Pb = gray; S = yellow; Cl = green.
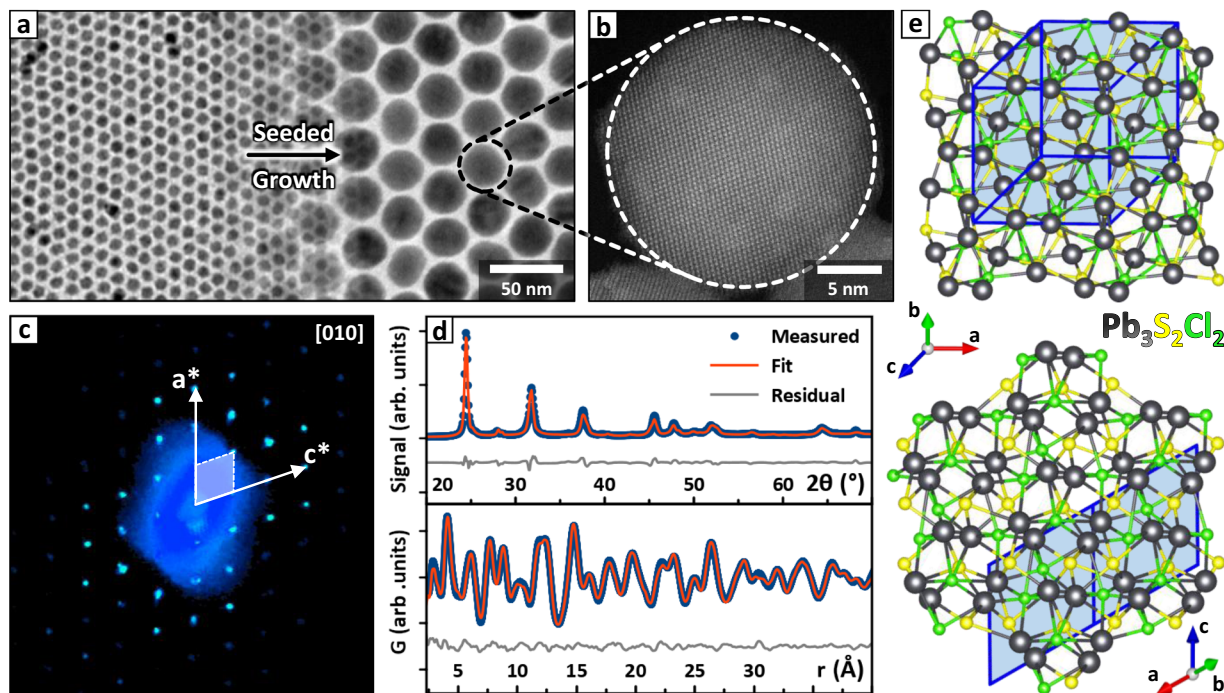
Fig. 2 Pb₃S₂Cl₂ NCs structure solution. a Pb$_3$S$_2$Cl$_2$ NCs as synthesized (left) and after the accretion process (right). **b** HAADF-STEM image of a Pb$_3$S$_2$Cl$_2$ NC. **c** [010] projection of the Pb$_3$S$_2$Cl$_2$ reciprocal lattice measured by 3D-ED, together with a representation of the reciprocal lattice axes and unit cell. **d** XRPD (top) and PDF (bottom) fits obtained by refining the Pb$_3$S$_2$Cl$_2$ structure in the Cc space group (experimental data = blue, fit curves = orange, residuals = gray). The XRPD profiles are plotted in the Cu-K$_\alpha$ 2θ scale to ease the comparison with lab-grade diffraction patterns. **e** Two views of the Cc monoclinic Pb$_3$S$_2$Cl$_2$ structure are shown along the high symmetry directions of the corresponding pseudocubic cell ([100] top, [111] bottom). A projection of the monoclinic cell is overlaid in blue, and the directions of the corresponding lattice vectors are indicated by labeled arrows. Atoms color code: Pb = gray; S = yellow; Cl = green. Source data for **d** are provided as a Source Data file.

compatible with our previously advanced hypothesis of a Pb$_3$S$_2$Cl$_2$ compound[25]. However, the X-Ray Powder Diffraction (XRPD) pattern could not be fitted based on the supposedly related Pb$_3$Se$_2$Br$_2$ cubic prototype[25,31], suggesting a different structure. Therefore, we exploited a combination of techniques to solve it. First, we performed a single-NC 3D Electron Diffraction (3D-ED)[37] experiment to identify the unit cell parameters and a list of possible space groups (Fig. 2c). For some of them we also produced ab-initio solutions; however, a definitive structural model could not be obtained due to the small size of the NCs, which made the integrated intensity of the diffraction spots inaccurate. Thus, we exploited the information from 3D-ED to repeat the ab-initio structure solution from XRPD data with the software EXPO2014[38], eventually obtaining a model close to the cubic Pb$_3$Se$_2$Br$_2$ in terms of connectivity, but with a lower symmetry. Finally, we refined this model in both reciprocal and direct spaces on data collected at the Brookhaven National Laboratory synchrotron, on setups optimized for XRPD and Pair Distribution Function (PDF) experiments respectively (Fig. 2d).

The solution was found in the monoclinic Cc space group (Fig. 2e, see Supplementary Discussion, section 2 for details), capturing deviations from the Pb$_3$Se$_2$Br$_2$ cubic prototype that are likely due to the small ionic radii of S^{2-} and Cl$^-$. Density Functional Theory calculations (DFT, see Supplementary Discussion, section 3) confirmed that as a bulk crystal the monoclinic Pb$_3$S$_2$Cl$_2$ would be more stable than a hypothetical cubic polymorph by 164 kcal/mol. The ionic radii are also likely to play a major role in favoring the Pb$_3$S$_2$Cl$_2$ phase over Pb$_4$S$_3$Cl$_2$ for free-standing lead sulfochloride NCs. Indeed, Pb$_3$E$_2$X$_2$ appears to be favored if $r_{E^{2-}}/r_{X^-} \approx 1$ (Se^{2-}/Br$^-$ = 1.01; S^{2-}/Cl$^-$ = 1.02)[31], while $r_{E^{2-}}/r_{X^-} < 1$ favors Pb$_4$E$_3$X$_2$ (S^{2-}/Br$^-$ = 0.94; S^{2-}/I$^-$ = 0.84)[25,30,39]. Indeed, in both structures Pb^{2+} is surrounded by

eight anions, and S^{2-} features a distorted octahedral coordination. Conversely, the coordination of the halide changes: in Pb$_3$S$_2$Cl$_2$ the smaller Cl$^-$ ions share the same octahedral coordination as S^{2-}, while the larger Br$^-$ and I$^-$ ions in Pb$_4$S$_3$X$_2$ are surrounded by seven Pb^{2+} ions in a pentagonal bipyramidal configuration. The reason is likely that bulkier anions can accommodate an enlarged coordination environment. Interestingly, Pb$_3$S$_2$Cl$_2$ is the only lead chalcohalide where Cl$^-$ is coordinated by an octahedron of Pb^{2+} ions. Such coordination has been recently proposed on the surface of PbS NCs synthesized in excess of PbCl$_2$ to account for the formation of a Cl-rich shell that improves the optical properties[40–43], suggesting that these NCs might be passivated by a layer of some lead sulfochloride compound. For further comparisons between the structures of Pb$_3$S$_2$Cl$_2$ and Pb$_3$S$_2$X$_2$ compounds see Supplementary Discussion, section 4, which includes the structure refinements of Pb$_4$S$_3$Br$_2$ and Pb$_4$S$_3$I$_2$ NCs and a comparison of PDF profiles by RootProf[44].

Compatibility of lead sulfochlorides with CsPbX₃. Our prior studies demonstrated that the lead sulfobromide Pb$_4$S$_3$Br$_2$ can grow epitaxially on lead halide perovskite domains[26], suggesting that other isostructural compounds, i.e., Pb$_4$S$_3$I$_2$ and a hypothetical Pb$_4$S$_3$Cl$_2$, would do the same. Conversely, the Pb$_3$S$_2$Cl$_2$ structure we hereby solved is remarkably different from that of the Pb$_4$S$_3$X$_2$ compounds, to the point that the epitaxial compatibility with CsPbX$_3$ would be lost. This prompted us to think that the synthesis of a sulfochloride/perovskite heterostructure would produce domains of the yet unknown compound Pb$_4$S$_3$Cl$_2$ instead. Indeed, the Pb$_4$S$_3$X$_2$/CsPbX$_3$ match, regardless of the halide, is strictly structure specific. First, both the chalcohalide and the perovskite share a plane of Pb^{2+} ions arranged in a square grid, which serves
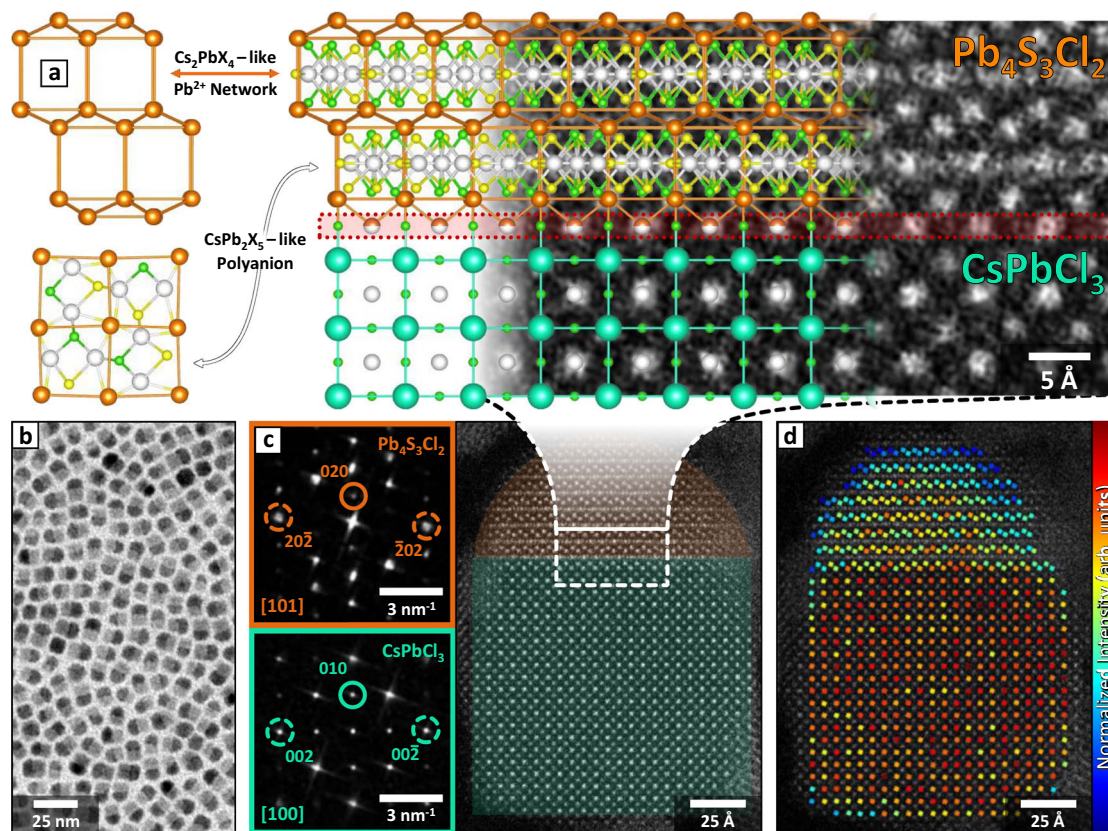
Fig. 3 Pb$_4$S$_3$Cl$_2$/CsPbCl$_3$ epitaxial heterostructures. a On the left, models of the Cs$_2$PbX$_4$-like Pb^{2+} subnetwork (orange Pb^{2+}) and of the CsPb$_2$X$_5$-like [Pb$_2$S$_3$Cl$_2$]$^-$ polyanion (white Pb^{2+}, yellow S^{2-}, green Cl$^-$) found in Pb$_4$S$_3$Cl$_2$. On the right, model of the Pb$_4$S$_3$Cl$_2$/CsPbCl$_3$ epitaxial interface superimposed on a close-up view of **c**, highlighting the continuity of the Pb^{2+}/Cs$^+$ cationic subnetwork. The Pb$_4$S$_3$Cl$_2$ structure has been represented by adapting the Pb$_4$S$_3$Br$_2$ structure. Atoms color code: Cs = cyan; Pb = orange/white; S = yellow; Cl = green. **b** Low resolution TEM image of as-synthesized Pb$_4$S$_3$Cl$_2$/CsPbCl$_3$ heterostructures. **c** HAADF-STEM image of a single Pb$_4$S$_3$Cl$_2$/CsPbCl$_3$ heterostructure. Insets: FFTs of the Pb$_4$S$_3$Cl$_2$ (top) and CsPbCl$_3$ (bottom) domains. The spots circled in a solid line correspond to planes parallel to the heterostructure interface and to each other; those circled in a dashed line are instead perpendicular to the interface and share similar periodicities, ensuring the match of the two lattices. **d** Column intensity map of the Pb-containing columns in the perovskite phase and of the Pb columns in the Cs$_2$PbX$_4$-like subnetwork of the Pb$_4$S$_3$Cl$_2$ domain. The color in the intensity map correlates with the total intensity scattered from the corresponding atomic column (red = higher intensity; blue = lower intensity). The map is compatible with the interface model depicted in Fig. 3a, and highlights the preservation and merging of the cationic subnetwork of the two phases across the interface. Source data for **d** are provided as a Source Data file.

as an interface between the two domains (in red in Fig. 3a, right)[26]. No such plane can be found in Pb$_3$S$_2$Cl$_2$. Moreover, Pb$_4$S$_3$X$_2$ shares deep similarities with some of the Cs-Pb-X phases and the heterostructures they form with CsPbX$_3$, which are easily overlooked at first sight. Indeed, the Cs-Pb-X compounds share a common cationic subnetwork of Cs$^+$ ions, which in Cs-Pb-X/Cs-Pb-X heterostructures is preserved across the interface and ensures the lattice compatibility[32]. Remarkably, similar connectivity is found across the Pb$_4$S$_3$X$_2$/CsPbX$_3$ interface. Relevant examples for our discussion are the CsPb$_2$X$_5$/CsPbX$_3$ heterostructures[45,46]. In CsPb$_2$X$_5$, the Cs$^+$ subnetwork encloses layers of [Pb$_2$X$_5$]$^-$ bidimensional polyanions[32]. Remarkably, Pb$_4$S$_3$X$_2$ is almost isostructural to CsPb$_2$X$_5$, being formed by a Pb^{2+} subnetwork enclosing [Pb$_2$S$_3$X$_2$]$^-$ polyanions of identical geometry. The only difference is the presence of an extra layer of Pb^{2+} ions in between each polyanion, that is needed to maintain the charge balance (Fig. 3a, left). This makes the Pb^{2+} subnetwork of Pb$_4$S$_3$X$_2$ resemble that of another Cs-Pb-X phase, namely Cs$_2$PbX$_4$. Consequently, the cationic subnetwork of Pb$_4$S$_3$X$_2$ is similar to that found in Cs-Pb-X compounds and can find its natural prosecution in the CsPbX$_3$ perovskite (Fig. 3a, right), ensuring the stability of the interface and remarking the pivotal role of ionic subnetworks in the formation of colloidal heterostructures. Deeper insights into

the heterostructure interface connectivity and the similarities with Cs-Pb-X/Cs-Pb-X heterostructures can be found in the Supplementary Discussion, section 5.

Synthesis of Pb$_4$S$_3$Cl$_2$/CsPbCl$_3$ heterostructures. To test whether the natural affinity of the Pb$_4$S$_3$X$_2$ phases for lead halide perovskites would lead to the formation of Pb$_4$S$_3$Cl$_2$, we adapted our previously reported method to attempt the synthesis of Pb$_4$S$_3$Cl$_2$/CsPbCl$_3$ heterostructures[26]. In the first step of the procedure, CsPbCl$_3$ nanoclusters, prepared separately, were reacted with elemental sulfur in the presence of lead oleate and dodecanethiol at 200 °C, indeed producing heterostructures. The resulting particles were recovered through antisolvent precipitation, and then treated with a solution of PbCl$_2$, oleylamine, and oleic acid to restore their colloidal stability (see Supplementary Discussion, section 6). The heterostructures were homogeneous in terms of size and shape (Fig. 3b), and no single-phase perovskite or sulfochloride NCs were observed.

High-Angle Annular Dark-Field Scanning TEM (HAADF-STEM) showed that the heterostructures were composed of two highly crystalline domains jointed along a flat interface spanning across the entire nanoparticle (Fig. 3a, c). As expected, the fast

Fourier transform (FFT) of the HAADF-STEM image revealed that the $CsPbCl_3$ domain matches with the perovskite structure, while that of the lead sulfochloride domain is incompatible with $Pb_3S_2Cl_2$. Instead, the unit cell parameters and the overall FFT symmetry match with what is expected for a $Pb_4S_3X_2$ domain based on our previous observations on $Pb_4S_3Br_2/CsPbX_3$ heterostructures (insets of Fig. 3c)[26]. Such phase selectivity was granted by the transformation of $CsPbCl_3$ nanoclusters into NCs during the early stages of the reaction[26]. The perovskite NCs then acted as phase-selective heterogeneous nucleation seeds for $Pb_4S_3Cl_2$, providing a significant advantage over the homogeneous nucleation of $Pb_3S_2Cl_2$, which was indeed suppressed.

The predicted structure of the $Pb_4S_3Cl_2/CsPbCl_3$ interface, superimposed in Fig. 3a to a high-resolution HAADF-STEM image of the heterostructure, was further confirmed by highlighting the Pb-containing atomic columns involved in the Pb^{2+} cationic subnetwork through the quantitative analysis of HAADF-STEM images (Fig. 3d). Indeed, it is worth noting that a prosecution of the chalcohalide-Pb^{2+} subnetwork, identified in Fig. 3a with the perovskite-Cs^+ subnetwork in analogy with the $CsPb_2X_5/CsPbX_3$ heterostructures, can also be found in the Pb^{2+} subnetwork of the perovskite domain, as it shares the same symmetry as the Cs^+ one (see Supplementary Discussion, section 5 for details).

Selective etching of the $CsPbCl_3$ domain. Our templated synthesis approach could be pushed a step further as we took advantage of the solubility of $CsPbCl_3$ in polar solvents to selectively etch the perovskite domains and recover phase-pure $Pb_4S_3Cl_2$ NCs (Fig. 4). Briefly, the heterostructures dispersed in hexane were first treated with oleylamine to improve the colloidal stability of the etched NCs in nonpolar media. Then, we added to the dispersion an equal volume of dimethylformamide (DMF), and the resulting mixture was vortexed for 30 s, forming an emulsion. After its complete separation, DMF was removed, and predried oleic acid was introduced in the NCs hexane dispersion. Subsequently, the particles were recovered through antisolvent precipitation followed by a centrifugation, and redispersed in toluene for further use. The procedure yielded remarkably uniform $Pb_4S_3Cl_2$ NCs, whose structure was confirmed via high-resolution HAADF-STEM imaging and analysis of the lattice by means of FFTs. Interestingly, the NCs appeared to be sphere-shaped despite the original chalcohalide domains in the heterostructures being hemispherical. We attribute this change of morphology to the need of lowering the surface energy of the extended and non-passivated facet left after the dissolution of the perovskite. It is likely that the excess ions released by the etching process will recrystallize on the chalcohalide domains, thus reshaping them into a more stable spherical morphology. See Supplementary Discussion, section 7 for details on the etching of heterostructures.

Optoelectronic properties of lead sulfochloride NCs. Obtaining both $Pb_3S_2Cl_2$ and $Pb_4S_3Cl_2$ NCs, and the latter both in the form of free-standing NCs and heterostructures with $CsPbCl_3$, gave us the opportunity to investigate the impact of stoichiometry, structure, and presence of a heterojunction on the optoelectronic properties of lead sulfochlorides. Figure 5 summarizes the experimental results, along with data from DFT calculations. The free-standing $Pb_3S_2Cl_2$ and $Pb_4S_3Cl_2$ NCs exhibited basically overlapping and featureless absorption spectra, with onset at ~1.8 eV (~690 nm, Fig. 5a, solid blue and orange plots). The Tauc plot analysis suggested an indirect band gap of ~1.8 eV in both cases, in agreement with the DFT predictions (see Supplementary Discussion, sections 3 and 8). This is in stark contrast with the
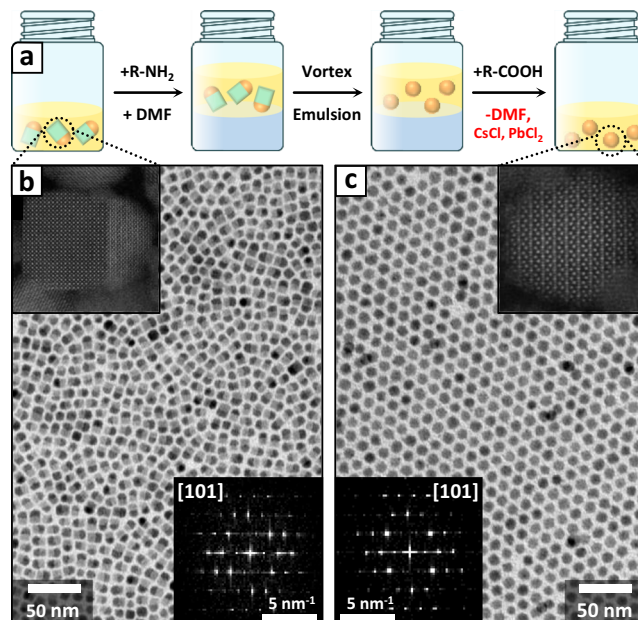

Fig. 4 Selective etching of $Pb_4S_3Cl_2/CsPbCl_3$ heterostructures. a Scheme of the DMF-assisted etching procedure developed to transform the $Pb_4S_3Cl_2/CsPbCl_3$ heterostructures into $Pb_4S_3Cl_2$ NCs in the presence of surfactants (R-NH_2 = oleylamine, R-COOH = oleic acid). The cyan cubes and the orange spheres represent the $CsPbCl_3$ and the $Pb_4S_3Cl_2$ domains of the heterostructures, respectively. **b** TEM image of the starting heterostructures. The top inset shows an HAADF-STEM image of one heterostructure prior to the etching, while the bottom inset shows the FFT of the chalcohalide domain of the same image. **c** TEM image of the etched NCs. The top inset shows an HAADF-STEM image of one NC after the etching, while the bottom inset shows the FFT of the same image. The two FFTs demonstrate that the $Pb_4S_3Cl_2$ domains retain the same crystal structure before and after the etching procedure.

direct bandgap observed for lead chalcogenides (PbE) and many lead halides (e.g., $CsPbX_3$), remarking that the electronic properties of lead chalcohalides are not straightforwardly related to those of chemically similar compounds. A comparable absorption profile was found in the heterostructures spectrum, combined with the blunt absorption edge of the direct-gap $CsPbCl_3$ domain (~3.1 eV = 400 nm[24,47], Fig. 5a, solid black plot). Such edge was instead sharp for free-standing $CsPbCl_3$ NCs (Fig. 5a, solid cyan plot), suggesting an intimate electronic connection between the two domains in the heterostructures. This was further supported by the almost complete suppression of the $CsPbCl_3$ photoluminescence (PL) when the perovskite domain was involved in the heterojunction (Fig. 5b, inset).

DFT calculations suggested that the cause for the PL quenching was the nearly type-I band alignment between $Pb_4S_3Cl_2$ and $CsPbCl_3$ (Fig. 5e, see also Supplementary Discussion, section 3). Interestingly, this contrasts with the structurally equivalent $Pb_4S_3Br_2/CsPbBr_3$ heterostructures investigated in our previous work, which were instead identified as quasi-type-II junctions[26]. Indeed, the molecular orbitals corresponding to the band edge states of the heterostructures are strongly localized on the sulfochloride domain (Fig. 5f). It is worth noting that the predicted type-I alignment should promote the migration of photocarriers into the sulfochloride domain of the heterostructure. Indeed, the decay of the barely detectable PL of $CsPbCl_3$ in the heterostructures was strongly accelerated if compared with that of free-standing $CsPbCl_3$ NCs (τ_{avg} ~8 ps vs ~18 ps, Fig. 5b).
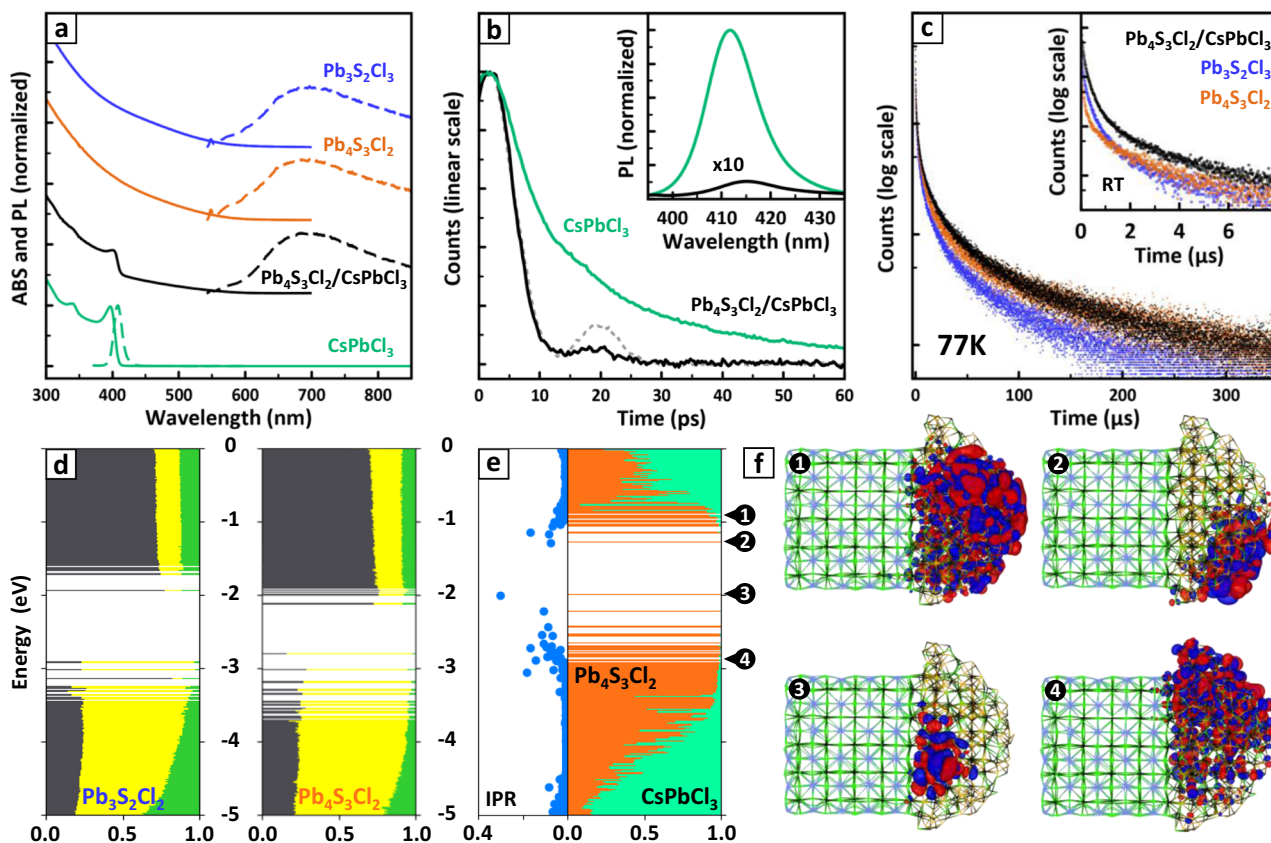
Fig. 5 Optoelectronic properties of lead sulfohalide NCs and Pb₄S₃Cl₂/CsPbCl₃ heterostructures. a Absorption (ABS, solid lines) and photoluminescence (PL, dashed lines) spectra of free-standing Pb₃S₂Cl₃, Pb₄S₃Cl₂, CsPbCl₃ NCs and of Pb₄S₃Cl₂/CsPbCl₃ heterostructures. The CsPbCl₃ NCs were prepared for comparison purposes by heating the CsPbCl₃ precursor nanoclusters (see Supplementary Discussion, section 6). **b** Decay curves of the ~410 nm PL from CsPbCl₃ as free-standing NCs and in the Pb₄S₃Cl₂/CsPbCl₃ heterostructures. The dashed gray line is the time response of the experimental setup. Inset: PL spectra of CsPbCl₃ as free-standing NCs and in the heterostructures, showing a drastic quenching in the latter case. The PL intensity of the heterostructures is multiplied ×10 to make it more visible. The slight redshift of the heterostructure PL maximum is likely due to the relaxation of quantum confinement of the perovskite domain caused by the partial delocalization of the exciton in the chalcohalide domain. **c** Decay curves of the ~1.8 eV (~690 nm) emission of the three samples at room temperature and at 77 K (inset). Color code for **a**–**c**: cyan = CsPbCl₃, blue = Pb₄S₃Cl₂, orange = Pb₃S₂Cl₃, black = Pb₄S₃Cl₂/CsPbCl₃ heterostructures. **d** Electronic structure of free-standing Pb₃S₂Cl₃ (left) and Pb₄S₃Cl₂ (right) NC models computed at the DFT/PBE level of theory. The color code indicates the elemental contribution to each molecular orbital (Pb = gray; S = yellow; Cl = green). **e** Electronic structure of the Pb₄S₃Cl₂/CsPbCl₃ heterostructure model computed at the DFT/PBE level of theory, color coded by domain (Pb₄S₃Cl₂ = orange; CsPbCl₃ = cyan). The Inverse Participation Ratio (IPR, left panel) quantifies the degree of localization of a state ($1/N_{atoms}$ = completely delocalized; 1 = localized on one single atom), and indicates that most of the states surrounding the band gap are localized trap states. **f** Representation of molecular orbitals corresponding to band edge delocalized states (1,4) and to band edge trap states (2,3). In both cases, the band edge states are localized on the Pb₄S₃Cl₂ domain. Source data for **a**–**e** are provided as a Source Data file.

Owing to the relaxation of the momentum conservation at the nanoscale, both the free-standing sulfochlorides and the heterostructures exhibited a broad PL peak at ~1.8 eV (~690 nm, see Fig. 5a, dashed lines), indicating in all the cases a sulfochloride band edge emission. Such emission was negligible at room temperature (PLQY < 1%) due to the efficient thermal quenching. However, lowering the temperature to 77 K resulted in a ~100-fold intensification of the PL, accompanied in the case of heterostructures by a brightening of the residual, yet still negligible, CsPbCl₃ emission. In all three cases, the PL kinetics of the lead chalcohalides was markedly non-exponential, with a dominant sub-microsecond drop followed by a slower decay (Fig. 5c). The process was slightly slower in the heterostructures with respect to both free-standing Pb₃S₂Cl₃ and Pb₄S₃Cl₂ NCs, suggesting that the CsPbCl₃ domain might suppress some trapping losses by passivating part of the sulfochloride domain surface. This is also consistent with our observation of a more intense PL. At low temperatures, all the PL decays became

substantially longer. Fitting the dataset with an Arrhenius function yielded for all the samples an activation energy of ~15 meV. Remarkably, the spectral shape of all samples followed a nearly identical trend with the temperature, showing a progressive shift to ~1.5 eV (~827 nm) and a band narrowing, further corroborating the strong similarities between the optoelectronic properties of these three systems. See Supplementary Discussion, section 8 for details on the spectroscopic characterizations.

In general, our analysis indicates that the properties of lead sulfochlorides are largely independent of both stoichiometry and structure. This completes our preliminary observations on Pb₄S₃Br₂ and Pb₄S₃I₂ NCs, that shared nearly identical absorption spectra despite containing different halides[25]. We rationalized such behavior as a consequence of two factors. First, in these materials the band edge states feature a prominent participation of Pb²⁺ and S²⁻, while the halides mostly contribute to states buried deep in the valence band, making the electronic properties almost halide-

insensitive. Second, regardless of the structure of the specific chalcohalide, the geometry and connectivity of the coordination polyhedra surrounding both Pb^{2+} and S^{2-} is the same, making the electronic properties basically structure-insensitive.

Discussion

In this work, we have exploited the epitaxial templating effect of $CsPbCl_3$ to control the synthesis of lead sulfohalide NCs through the formation of $Pb_4S_3Cl_2/CsPbCl_3$ heterostructures. Indeed, while a direct synthesis approach (i.e., in the absence of $CsPbCl_3$ acting as a template) yielded $Pb_3S_2Cl_2$ NCs, only the selective etching of the heterostructures perovskite domain allowed us to recover free-standing $Pb_4S_3Cl_2$ NCs. This ultimately means that we could select the reaction product between two competing phases, a problem of great relevance in the synthesis of colloidal inorganic nanomaterials. Both the obtained lead sulfochlorides shared remarkably similar optoelectronic properties. This, combined with our previous observation on bromine- and iodine-based sulfohalides[25], suggests that lead sulfohalide compounds are mostly stoichiometry- and structure-insensitive. Interestingly, the discovery of the $Pb_3S_2Cl_2$ structure demonstrates that Cl^- in lead chalcohalides can be coordinated by an octahedron of Pb^{2+} ions, differently from Br^- and I^-. This supports the recent observations of a $PbCl_x$-rich shell on the surface of PbS NCs synthesized using $PbCl_2$ as a precursor, a condition that is remarkably similar to our synthetic protocol and might indeed lead to the formation of a lead sulfochloride surface layer[40−43].

We remark that our use of perovskite NCs as disposable and phase-selective epitaxial templates parallels that of reaction-directing groups in traditional organic chemistry and catalysis[27], and allowed us to design the phase-selective synthesis of two yet unknown materials ($Pb_3S_2Cl_2$ and $Pb_4S_3Cl_2$) based on structural considerations only. Such an approach to a deterministic synthesis of NCs may be extended to other phases with known or predictable epitaxial relations, taking advantage of the vast library of already reported nanomaterials as starting templates. For example, in the field of chalcohalides it might lead to yet unknown selenium- and tellurium-based materials, or even to compounds where the halide is replaced by pseudohalide ions (e.g., CN^- and SCN^-). In conclusion, we envision that our phase-selective templating approach will open new routes for the colloidal syntheses of nanomaterials which are now hindered by an excessive activation energy for the homogeneous nucleation, or by the competitive formation of undesired phases.

Methods

Chemicals. 1-octadecene (ODE, technical grade, 90%), oleic acid (OA, technical grade, 90%), oleylamine (OLA, technical grade, 70%), lead(II) chloride ($PbCl_2$, 98%), lead(II) bromide ($PbBr_2$, 98%), lead(II) iodide (PbI_2, 98%), lead(II) thiocyanate ($Pb(SCN)_2$, 99.5%), lead(II) acetate trihydrate ($Pb(OAc)_2 \cdot 3H_2O$, 99.99%), cesium(I) carbonate (Cs_2CO_3, 99%), dodecanethiol (DDT, 99.9%), and sulfur powder (S, 99.99%) were purchased from Sigma-Aldrich. All reagents were used as received without any further purification.

Synthesis: S-ODE stock solution for $Pb_3S_2Cl_2$ NCs. 0.064 g (2 mmol) of S powder were mixed with 10 mL of ODE (pre-degassed at 120 °C under vacuum for an hour) in a 20 mL glass vial inside a glove box filled with N_2. The resulting mixture was sonicated until the complete dissolution of the sulfur powder.

Synthesis: $Pb_3S_2Cl_2$ nanocrystals (NCs). 0.21 g of $PbCl_2$ (0.8 mmol) were solubilized at 120 °C in a mixture of 2 mL of OLA, 2 mL of OA and 20 mL of ODE in a 100 mL flask. The solution was heated up to 170 °C, and 2 mL of the S-ODE stock solution, pre-heated at 150 °C, were swiftly injected. The NCs formed ~10–30 s after the injection, as revealed by the color change of the solution from pale yellow to red. After 1 min, the reaction was quenched by cooling the flask with a room-temperature water bath. The NCs were recovered by adding 40 mL of ethyl acetate, followed by a centrifugation at 6000 rpm (~2940 × g) for 5 min. The precipitate was discarded, and the supernatant was suspended in hexane or toluene. If needed, the sample could be washed multiple times by adding ethyl acetate and

repeating the centrifugation. The maximum diameter for $Pb_3S_2Cl_2$ NCs obtained by direct synthesis was 7–8 nm (see Supplementary Discussion, section 1).

Synthesis: accretion of larger $Pb_3S_2Cl_2$ NCs. Larger NCs were obtained through a seeded growth approach, performed by using as starting seeds $Pb_3S_2Cl_2$ NCs prepared as detailed above. A stock solution of reagents was prepared by dissolving 0.2966 g of $PbCl_2$ (1.06 mmol) and 0.6898 g of $Pb(SCN)_2$ (2.13 mmol) in a mixture of 4 mL of OLA, 4 mL of OA, and 40 mL of ODE in a 100 mL flask at 120 °C. During its preparation, the stock solution must not exceed this temperature to avoid the thermal decomposition of the thiocyanate, which would cause the nucleation of PbS NCs[25]. Once the two solids were completely solubilized, the stock solution was cooled to room temperature, filtered with a 0.2 μm PTFE syringe filter, and loaded on a syringe pump. Then, a crude $Pb_3S_2Cl_2$ reaction mixture in ODE was obtained by following the procedure detailed in the previous paragraph up to before the addition of ethyl acetate. 12 ml of such solution were heated to 170 °C, and the stock solution of $PbCl_2$ and $Pb(SCN)_2$ was added dropwise at a controlled rate of 10 mL/h with the help of a syringe pump. Finally, the reaction mixture was washed with ethyl acetate as described in the previous paragraph, and the NCs were suspended in hexane. A last step of filtration performed with a 0.2 μm PTFE syringe filter allowed to remove any impurity of PbS that may have formed during the accretion process. The so-obtained $Pb_3S_2Cl_2$ NCs measured 29.5 ± 2.0 nm on average, and were used to solve the structure of the material by a combination of 3D-ED, XRPD, and PDF experiments. See Supplementary Discussion, section 1 for additional details on the accretion process.

Synthesis: $Pb_4S_3Br_2$ (or $Pb_4S_3I_2$) NCs. NCs of $Pb_4S_3Br_2$ (and $Pb_4S_3I_2$) were prepared following our previously published method[25]. In short, 0.2 mmol of $PbBr_2$ (or PbI_2) and 0.2 mmol of $Pb(SCN)_2$ where dissolved in a mixture of 10 mL ODE and 250 μL of OLA and OA at 120 °C in a 25 mL three-necked flask. Then, the solution was quickly heated (~20 °C/min) and started turning from light-yellow to bloody red above 150 °C while the NCs nucleated and grew. The reaction was quenched by cooling the flask in a water bath. The NCs were recovered by simple centrifugation or by ethyl-acetate assisted precipitation followed by centrifugation (6000 rpm for 5 min in both cases, ~2940 × g). The so-obtained $Pb_4S_3Br_2$ and $Pb_4S_3I_2$ NCs were used to refine the structure of both materials by XRPD and PDF experiments (see Supplementary Discussion, section 4).

Synthesis: Cs-oleate precursor for $CsPbCl_3$ nanoclusters. The Cs-oleate precursor was prepared by increasing the concentration of oleic acid in comparison to our previously reported method[26]. In a typical synthesis, Cs_2CO_3 (0.652 g, 2 mmol), OA (5 mL, 15 mmol) and ODE (17.5 mL) were loaded into a 50 mL 3-neck flask, dried for 1 h at 110 °C and then heated under N_2 to 150 °C until the solution turned clear. The resulting mixture was transferred into a N_2 filled glass vial, which was stored inside a glovebox for further use.

Synthesis: $PbCl_2$ stock solution for heterostructures. $PbCl_2$ powder (0.556 g, 2 mmol), OA (5 mL), and OLA (5 mL) were mixed with ODE (30 mL) in a 100 mL three neck round bottom flask. The reaction mixture was dried/degassed under vacuum for 15 min at 110 °C. Then, the flask was filled with N_2 and the temperature was raised to 150 °C. After complete dissolution of $PbCl_2$ salt, the solution was cooled down to room temperature (25 °C) and transferred into a N_2-filled glass vial.

Synthesis: $Pb(OA)_2$ stock solution for heterostructures. The lead oleate stock solution was prepared following our previously reported method[26]. Briefly, $Pb(OAc)_2 \cdot 3H_2O$ powder (0.76 g, 2 mmol) and OA (1.3 mL), were mixed with ODE (18.7 mL) in a 50 ml three neck round bottom flask. The reaction mixture was degassed under vacuum for 1 h at 110 °C and then heated under N_2 to 150 °C until all $Pb(OAc)_2 \cdot 3H_2O$ reacted with OA. Thereafter, the solution was cooled down to room temperature (25 °C) and transferred into N_2-filled glass vials.

Synthesis: $CsPbCl_3$ nanoclusters. $CsPbCl_3$ nanoclusters were synthesized following a previously reported method[26]. Briefly, 4 mL of the above-mentioned $PbCl_2$ stock solution were transferred into the N_2 filled 20 ml glass vial. Thereafter, 0.25 mL of the Cs-oleate precursor were injected into the $PbCl_2$ stock solution at 40 °C and the resulting mixture was kept under stirring for 20 min. After about 20 min, the mixture (turbid white) was centrifuged at 8000 rpm (~3935 × g) for 5 min, the supernatant was discarded, and the precipitate was redispersed in 0.9 mL of degassed ODE.

Synthesis: $Pb_4S_3Cl_2/CsPbCl_3$ heterostructures. 4.0 mL of degassed ODE were added to a 20 mL glass vial under N_2. The vial was heated to 200 °C, and 100 μL of the above-mentioned $Pb(OA)_2$ solution and 20 μL DDT (diluted in 200 μL predried ODE) were added into the reaction system. Then, the mixture of S (0.1 mL) and $CsPbCl_3$ nanoclusters (0.9 mL) was rapidly injected into the reaction mixture. The reaction was allowed to proceed for 5 min and was subsequently quenched by immersing the vial in an ice and water bath. The crude solution was then

centrifuged by adding methyl acetate (with volume ratio of 1 to 1) and the precipitate was redispersed in toluene. See Supplementary Discussion, section 6 for details.

Synthesis: surface treatment of heterostructures. A $PbCl_2$ solution, separately prepared by dissolving $PbCl_2$ salt (1 mmol) in ODE (15 mL) in the presence of oleic acid (2.5 mL) and oleylamine (2.5 mL), was added to the toluene dispersion containing the heterostructures, and the mixture was vortexed for 1 min. Then, the solution was centrifuged by adding methyl acetate and the precipitate was redispersed in hexane or toluene for further use. The role of this treatment is to reconstruct the surface of the $CsPbCl_3$ perovskite domains after the antisolvent-assisted precipitation, and to ensure the long-term colloidal stability of the sample.

Synthesis: $CsPbCl_3$ NCs. 4.0 mL of ODE were added to a 20 mL glass vial under air and heated to 150 °C, then 1.0 mL of the above-mentioned seed cluster solution ($CsPbCl_3$, without S-ODE) was swiftly injected. The mixture was annealed for 5 min and subsequently cooled down by using an ice water bath. The resulting mixture was centrifuged at 8000 rpm ($\sim$3935 $\times$ g) for 5 min, the supernatant was discarded, and the precipitate was dispersed in 4 mL of toluene.

Synthesis: etching of $Pb_4S_3Cl_2/CsPbCl_3$ heterostructures. 1 mL of heterostructures dispersed in hexane (corresponding to one entire batch of heterostructures) was treated first with oleylamine (60 μL). Then, an equal volume ratio of dimethyl-formamide (DMF, 1 mL) was added to the heterostructures dispersion and the resulting mixture was vortexed for 30 s. After the complete phase separation of solvents (2–3 min), DMF was removed by using a syringe and pre-dried oleic acid (60 μL) was introduced in the hexane dispersion. Subsequently, the now etched NCs were centrifuged by adding methyl acetate (with 1 to 1 volume ratio) and were redispersed in toluene for further use. See Supplementary Discussion, section 7 for details.

Characterization: TEM. Bright-field TEM images of the samples were acquired with a JEOL-1100 transmission electron microscope operating at an acceleration voltage of 100 kV. The samples were prepared by drop casting diluted solutions of NCs or heterostructures onto carbon film-coated 200 mesh copper grids for low-resolution TEM.

Characterization: Lab-grade XRPD. Lab-grade XRPD analyses were performed in θ:2θ scan mode on a Panalytical Empyrean diffractometer, equipped with a 1.8 kW Cu-K$_\alpha$ ceramic anode working at 45 kV–40 mA and a PIXcel3D detector. XRPD data were acquired on samples in the form of dry powders or drop-casted solutions; the measurements were carried out in air at room temperature using a zero-diffraction silicon substrate.

Characterization: HAADF-STEM. High-resolution HAADF-STEM images were acquired with a probe-corrected cubed Thermo Fisher Scientific Themis Z Microscope operating at 300 kV with a probe semi-convergence angle of 20.5 mrad. For a quantitative analysis of the HAADF-STEM image, the intensities of the individual atomic columns in a single heterostructure were analyzed by using the StatSTEM software[48]. The color code in the intensity map correlates with the total intensity scattered from each atomic column. The intensity is calculated by fitting a Gaussian function to each atomic column: the intensity value of a column equals the volume of its Gaussian peak.

Characterization: 3D-ED. 3D-ED data were collected on a Zeiss Libra TEM operating at 120 kV and equipped with a LaB$_6$ source. Data were acquired in STEM mode after defocusing the beam to achieve a parallel illumination of the sample. A beam size of about 150 nm in diameter was obtained by inserting a 5 μm C2 condenser aperture. A mild illumination was adopted to avoid any alteration or amorphization of the sample, and to slow down the accumulation of organic contaminants. 3D-ED data were recorded with an ASI Timepix detector[49], which is able to detect single electrons and deliver a pattern that is virtually background-free. The camera length was 180 mm, with a theoretical resolution limit of 0.75 Å.

Characterization: synchrotron XRPD and PDF data collection. Synchrotron diffraction data were collected at the 28ID-2 beamline of the National Synchrotron Light Source (NSLS-II) of the Brookhaven National Laboratory with an X-ray energy of 67.17 keV (0.1846 Å) and a 0.5 mm × 0.5 mm beam size. A Perkin Elmer XRD 1621 digital imaging detector (2048 × 2048 pixels and 200 × 200 μm pixel size) was mounted orthogonal to the beam path in two positions: 228 mm and 1365 mm downstream of the sample. Samples of $Pb_3S_2Cl_2$, $Pb_4S_3Br_2$, and $Pb_4S_3I_2$ were measured in both setups, optimized for PDF and XRPD measurements, respectively. Lanthanum hexaboride (LaB$_6$) was measured as a standard material to calibrate the wavelength and the detector geometry, including the sample-to-detector distance. An empty capillary was measured for background estimation. Diffraction images were azimuthally integrated and converted into intensity profiles vs 2θ and vs momentum transfer $Q = 4\pi\sin\vartheta/\lambda_{X-ray}$ by using the FIT2D program[50]. PDF profiles were calculated up to interatomic distances r of 50 Å from

the Q profiles with the program PDFGetX3[51]. The parameters for PDF calculation (background subtraction, scale factor, minimum and maximum values of Q, degree of data-correction polynomial) were optimized on individual PDF profiles, to avoid large termination effects and preserve the signal to noise ratio. The Q_{max} values were 23.7 Å^{-1} for $Pb_3S_2Cl_2$ and 22.0 Å^{-1} for $Pb_4S_3Br_2$ and $Pb_4S_3I_2$.

Characterization: NCs structure solution and refinement. The solution and refinement of the $Pb_3S_2Cl_2$ NCs structure was performed through a combination of 3D-ED, XRPD, and PDF analyses. 3D-ED[37,52] was used to determine the starting unit cell parameters and a set of possible space groups. In the process, the software ADT3D[53] was used. XRPD was exploited to select the most promising space groups for the structure solution, extract the integrated intensities of reflections and perform the ab-initio structure solution by Direct Methods. In the process, the software EXPO2014[38] was used. Both XRPD and DFT data were exploited to refine the structure of NCs, by alternating the refinement in the direct (PDF) and reciprocal (XRPD) spaces. To analyze the PDF profiles, the PDFGUI[44,54,55] and DiffPy-CMI[16] software packages were used. The same refinement strategy was applied to $Pb_4S_3Br_2$ and $Pb_4S_3I_2$ NCs, while the structure solution step was not needed because the starting structure was already known[25,30]. All the crystal structure illustrations shown in this work were produced by using the software VESTA[56]. Additional details are provided in the Supplementary Discussion, section 4.

Characterization: optical spectroscopies. Absorbance and photoluminescence (PL) spectra of solution NCs and heterostructures were recorded on a Cary 500 spectrophotometer and Cary Eclipse spectrofluorometer, respectively. The spectra were measured in 10 × 10 mm quartz cuvettes. A wavelength of 350 nm was used for excitation during the collection of PL spectra. Regarding the extended spectroscopy: for PL and transient PL measurements, the samples were excited using a Laser-export Co. Ltd., frequency tripled, pulsed Nd:YAG laser at 3.49 eV (355 nm) and at 2.33 eV (532 nm) with 1 kHz repetition rate and detected respectively using an Hamamatsu Mini-Spectrometer and an Oriel Instrument Cornerstone 1/4 m monochromator coupled with a Hamamatsu UV–VIS photo-multiplier tube. Cryogenic Measurements were performed in a liquid nitrogen-cooled Oxford Instruments Limited cryostat.

DFT: comparison of monoclinic and cubic $Pb_3S_2Cl_2$ structures. To assess the impact of the cubic symmetry breaking on the stability of $Pb_3S_2Cl_2$ phase, we compared by DFT calculations the stability of the monoclinic $Pb_3S_2Cl_2$ structure that we solved with that of a hypothetic cubic $Pb_3S_2Cl_2$ structure. We performed this investigation on the corresponding $2 \times 2 \times 2$ supercells at the gamma point. In particular, we relaxed both atomic positions and cell parameters at the DFT level using the PBE exchange−correlation functional[57], and a double-ζ basis set plus polarization functions (DZVP) on all atoms as implemented in the CP2K 8.1 package[58]. Scalar relativistic effects were incorporated as effective core potentials in the basis set. With this approach, we determined that the monoclinic $Pb_3S_2Cl_2$ $2 \times 2 \times 2$ supercell is more stable than the prototypal cubic one by 164 kcal/mol.

DFT: calculations on NCs models. Both the structural relaxation and the electronic structure calculations of atomistic NCs models were carried out at the DFT/PBE/DZVP level of theory with CP2K. In order to identify any surface localized states that could trap charge carriers, we also computed the Inverse Participation Ratio (IPR) for chalcohalide and perovskite, both in the form of free-standing NCs and in the heterostructure. The IPR, as also demonstrated for other NCs[26,59], quantifies the orbital localization of a given molecular orbital and it is defined as:

$$IPR_i = \frac{\sum_\alpha |P_{\alpha,i}|^4}{(\sum_\alpha |P_{\alpha,i}|^2)^2}$$

Here, $P_{\alpha,i}$ represents the weight of molecular orbital i on a given atom α expanded in an atomic orbital basis. For finite systems, the IPR provides an estimate of the number of atoms that contribute to a given electronic state i. It can range from the inverse of the number of atoms in the system (when the wave function is distributed equally over all atoms in the system) to 1 in the case of states localized on single atoms. In other terms, IPR values very close to 0 identify delocalized states.

Data availability

References

1. Antonii, F. Panacea Aurea-Auro Potabile. (Bibliopolio Frobeniano, 1618).
2. Xia, Y., Xiong, Y., Lim, B. & Skrabalak, S. E. Shape-controlled synthesis of metal nanocrystals: simple chemistry meets complex physics? *Angew. Chem. - Int. Ed.* **48**, 60–103 (2009).
3. Lee, J., Zhang, S. & Sun, S. High-temperature solution-phase syntheses of metal-oxide nanocrystals. *Chem. Mater.* **25**, 1293–1304 (2013).
4. Cargnello, M., Gordon, T. R. & Murray, C. B. Solution-phase synthesis of titanium dioxide nanoparticles and nanocrystals. *Chem. Rev.* **114**, 9319–9345 (2014).
5. Tamang, S., Lincheneau, C., Hermans, Y., Jeong, S. & Reiss, P. Chemistry of InP nanocrystal syntheses. *Chem. Mater.* **28**, 2491–2506 (2016).
6. Lu, H., Carroll, G. M., Neale, N. R. & Beard, M. C. Infrared quantum dots: progress, challenges, and opportunities. *ACS Nano* **13**, 939–953 (2019).
7. Mcdonald, S. A. et al. Solution-processed PbS quantum dot infrared photodetectors and photovoltaics. *Nat. Mater.* **4**, 138–142 (2005).
8. Kolny-Olesiak, J. & Weller, H. Synthesis and application of colloidal $CuInS_2$ semiconductor nanocrystals. *ACS Appl. Mater. Interfaces* **5**, 12221–12237 (2013).
9. Gréboval, C. et al. Mercury chalcogenide quantum dots: material perspective for device integration. *Chem. Rev.* **121**, 3627–3700 (2021).
10. Murray, C. B., Norris, D. J. & Bawendi, M. G. Synthesis and characterization of nearly monodisperse CdE (E = S, Se, Te) semiconductor nanocrystallites. *J. Am. Chem. Soc.* **115**, 8706–8715 (1993).
11. Kim, S., Fisher, B., Eisler, H. J. & Bawendi, M. Type-II quantum dots: CdTe/CdSe(core/shell) and CdSe/ZnTe(core/shell) heterostructures. *J. Am. Chem. Soc.* **125**, 11466–11467 (2003).
12. Dey, A. et al. State of the art and prospects for halide perovskite nanocrystals. *ACS Nano* **15**, 10775–10981 (2021).
13. Akkerman, Q. A., Rainò, G., Kovalenko, M. V. & Manna, L. Genesis, challenges and opportunities for colloidal lead halide perovskite nanocrystals. *Nat. Mater.* **17**, 394–405 (2018).
14. Talapin, D. V., Lee, J. S., Kovalenko, M. V. & Shevchenko, E. V. Prospects of colloidal nanocrystals for electronic and optoelectronic applications. *Chem. Rev.* **110**, 389–458 (2010).
15. Losch, P. et al. Colloidal nanocrystals for heterogeneous catalysis. *Nano Today* **24**, 15–47 (2019).
16. Carey, G. H. et al. Colloidal quantum dot solar cells. *Chem. Rev.* **115**, 12732–12763 (2015).
17. Mitchell, M. J. et al. Engineering precision nanoparticles for drug delivery. *Nat. Rev. Drug Discov.* **20**, 101–124 (2020).
18. Park, Y. S., Roh, J., Diroll, B. T., Schaller, R. D. & Klimov, V. I. Colloidal quantum dot lasers. *Nat. Rev. Mater.* **6**, 382–401 (2021).
19. Toso, S., Baranov, D. & Manna, L. Metamorphoses of cesium lead halide nanocrystals. *Acc. Chem. Res.* **54**, 498–508 (2021).
20. Shamsi, J. et al. Colloidal CsX (X = Cl, Br, I) nanocrystals and their transformation to $CsPbX_3$ nanocrystals by cation exchange. *Chem. Mater.* **30**, 79–83 (2018).
21. Xu, J. et al. Ultrasonically-prepared copper-doped cesium halide nanocrystals with bright and stable emission. *Nanoscale* **13**, 9659–9667 (2021).
22. Klein, E., Lesyuk, R. & Klinke, C. Insights into the formation mechanism of two-dimensional lead halide nanostructures. *Nanoscale* **10**, 4442–4451 (2018).
23. Akkerman, Q. A. et al. Nearly monodisperse insulator Cs4PbX6 (X = Cl, Br, I) nanocrystals, their mixed halide compositions, and their transformation into $CsPbX_3$ Nanocrystals. *Nano Lett.* **17**, 1924–1930 (2017).
24. Protesescu, L. et al. Nanocrystals of cesium lead halide perovskites ($CsPbX_3$, X = Cl, Br, and I): novel optoelectronic materials showing bright emission with wide color gamut. *Nano Lett.* **15**, 3692–3696 (2015).
25. Toso, S. et al. Nanocrystals of lead chalcohalides: a series of kinetically trapped metastable nanostructures. *J. Am. Chem. Soc.* **142**, 10198–10211 (2020).
26. Imran, M. et al. Halide perovskite–lead chalcohalide nanocrystal heterostructures. *J. Am. Chem. Soc.* **143**, 1435–1446 (2021).
27. Rousseau, G. & Breit, B. Removable directing groups in organic synthesis and catalysis. *Angew. Chem. - Int. Ed.* **50**, 2450–2494 (2011).
28. Ider, A., Laval, J. P., Frit, B., Carré, J. & Bastide, J. P. Crystal structure of $PbTeF_6$. *J. Fluor. Chem.* **78**, 15–20 (1996).
29. Krebs, B. Die Kristallstrukturen von Pb_4SeBr_6, $Pb_5S_2J_6$ und $Pb_7S_2Br_{10}$. *ZAAC -. J. Inorg. Gen. Chem.* **396**, 137–151 (1973).
30. Ni, D., Guo, S., Yang, Z. S., Powderly, K. M. & Cava, R. J. $Pb_4S_3I_2$ –a high-pressure phase in the PbS-PbI system. *Solid State Sci.* **91**, 49–53 (2019).
31. Ni, D., Guo, S., Powderly, K. M., Zhong, R. & Cava, R. J. A high-pressure phase with a non-centrosymmetric crystal structure in the $PbSe–PbBr_2$ system. *J. Solid State Chem.* **280**, 106–111 (2019).
32. Toso, S., Baranov, D. & Manna, L. Hidden in plain sight: the overlooked influence of the Cs^+ substructure on transformations in cesium lead halide nanocrystals. *ACS Energy Lett.* **5**, 3409–3414 (2020).
33. Graham, C. et al. NaCl substrates for high-temperature processing and transfer of ultrathin materials. *Sci. Rep.* **10**, 7253 (2020).
34. Dish, N., Behera, R., Satyaprasad, A. & Gautam, A. Epitaxial growth of copper, gold, and silver on vicinal NaCl surfaces. *Appl. Surf. Sci.* **574**, 151643 (2022).
35. Dong, W. J., Kim, S., Park, J. Y., Yu, H. K. & Lee, J.-L. Ultrafast and chemically stable transfer of au nanomembrane using a water-soluble NaCl sacrificial layer for flexible solar cells. *ACS Appl. Mater. Interfaces* **11**, 30477–30483 (2019).
36. Lee, D. K. et al. Water-soluble epitaxial NaCl thin film for fabrication of flexible devices. *Sci. Rep.* **7**, 1–7 (2017).
37. Gemmi, M. et al. 3D electron diffraction: the nanocrystallography revolution. *ACS Cent. Sci.* **5**, 1315–1329 (2019).
38. Altomare, A. et al. EXPO2013: a kit of tools for phasing crystal structures from powder data. *J. Appl. Crystallogr.* **46**, 1231–1235 (2013).
39. Shannon, R. D. Revised effective ionic radii and systematic studies of interatomic distances in halides and chalcogenides. *Acta Crystallogr. Sect. A* **32**, 751–767 (1976).
40. Winslow, S. W., Liu, Y., Swan, J. W. & Tisdale, W. A. Quantification of a $PbCl_x$ shell on the surface of PbS nanocrystals. *ACS Mater. Lett.* **1**, 209–216 (2019).
41. Green, P. B. et al. PbS nanocrystals made using excess lead chloride have a halide-perovskite-like surface. *Chem. Mater.* **10**, 27 (2021).
42. Green, P. B., Li, Z. & Wilson, M. W. B. PbS nanocrystals made with excess $PbCl_2$ have an intrinsic shell that reduces their Stokes shift. *J. Phys. Chem. Lett.* **10**, 5897–5901 (2019).
43. Brittman, S. et al. Effects of a lead chloride shell on lead sulfide quantum dots. *J. Phys. Chem. Lett.* **10**, 1914–1918 (2019).
44. Caliandro, R. & Belviso, D. B. RootProf: software for multivariate analysis of unidimensional profiles. *J. Appl. Crystallogr.* **47**, 1087–1096 (2014).
45. Zheng, Y. et al. All-inorganic dual-phase halide perovskite nanorings. *Nano Res* **13**, 2994–3000 (2020).
46. Huang, Z. P. et al. In situ growth of 3D/2D ($CsPbBr_3$/$CsPb_2Br_5$) perovskite heterojunctions toward optoelectronic devices. *J. Phys. Chem. Lett.* **11**, 6007–6015 (2020).
47. Akkerman, Q. A. et al. Tuning the optical properties of cesium lead halide perovskite nanocrystals by anion exchange reactions. *J. Am. Chem. Soc.* **137**, 10276–10281 (2015).
48. De Backer, A., van den Bos, K. H. W., Van den Broek, W., Sijbers, J. & Van Aert, S. StatSTEM: an efficient approach for accurate and precise model-based quantification of atomic resolution electron microscopy images. *Ultramicroscopy* **171**, 104–116 (2016).
49. Gemmi, M. & Lanza, A. E. 3D electron diffraction techniques. *Acta Cryst. Sect. B Struct. Sci. Cryst. Eng. Mater.* **75**, 495–504 (2019).
50. Hammersley, A. P., Svensson, S. O., Hanfland, M., Fitch, A. N. & Häusermann, D. Two-dimensional detector software: from real detector to idealised image or two-theta scan. *High. Press. Res.* **14**, 235–248 (1996).
51. Juhás, P., Davis, T., Farrow, C. L. & Billinge, S. J. L. PDFgetX3: a rapid and highly automatable program for processing powder diffraction data into total scattering pair distribution functions. *J. Appl. Crystallogr.* **46**, 560–566 (2013).
52. Yun, Y., Zou, X., Hovmöller, S. & Wan, W. Three-dimensional electron diffraction as a complementary technique to powder X-ray diffraction for phase identification and structure solution of powders. *IUCrJ* **2**, 267–282 (2015).
53. Kolb, U., Krysiak, Y. & Plana-Ruiz, S. Automated electron diffraction tomography—development and applications. *Acta Crystallogr. Sect. B Struct. Sci. Cryst. Eng. Mater.* **75**, 463–474 (2019).
54. Farrow, C. L. et al. PDFfit2 and PDFgui: Computer Programs for Studying Nanostructure in Crystals. *J. Phys. Condens. Matter* **19**, 335219 (2007).
55. Juhás, P., Farrow, C. L., Yang, X., Knox, K. R. & Billinge, S. J. L. Complex modeling: a strategy and software program for combining multiple information sources to solve Ill posed structure and nanostructure inverse problems. *Acta Crystallogr. Sect. A Found. Adv.* **71**, 562–568 (2015).
56. Momma, K. & Izumi, F. VESTA: a three-dimensional visualization system for electronic and structural analysis. *J. Appl. Crystallogr.* **41**, 653–658 (2008).
57. Perdew, J. P., Burke, K. & Ernzerhof, M. Generalized gradient approximation made simple. *Phys. Rev. Lett.* **77**, 3865–3868 (1996).
58. Kühne, T. D. et al. CP2K: An electronic structure and molecular dynamics software package - Quickstep: efficient and accurate electronic structure calculations. *J. Chem. Phys.* **152**, 194103 (2020).
59. Houtepen, A. J., Hens, Z., Owen, J. S. & Infante, I. On the origin of surface traps in colloidal II–VI semiconductor nanocrystals. *Chem. Mater.* **29**, 752–761 (2017).

Author contributions
S.T. synthesized and characterized $Pb_3S_2Cl_2$, $Pb_4S_3Br_2$, and $Pb_4S_3I_2$ NCs. M.I. and Y.W. synthesized and characterized $Pb_4S_3Cl_2/CsPbCl_3$ heterostructures and $Pb_4S_3Cl_2$ NCs. S.T., E.M., A.M, R.C., and C.G. performed the structures solution and refinement. J.Z., F.Z., and I. I. performed the DFT simulations. N.S. performed the HRSTEM and the HAADF-STEM characterizations. A.P performed the spectroscopic characterizations. M.G., C.G., S. Brovelli, I.I, S. Bals, and L.M. coordinated the research work. S.T., L.M., and M.I. wrote the manuscript. All the authors contributed to reviewing and editing the manuscript.

Competing interests
The authors declare no competing interests.

Additional information
Supplementary information The online version contains supplementary material available at https://doi.org/10.1038/s41467-022-31699-1.

Correspondence and requests for materials should be addressed to Muhammad Imran, Anna Moliterni, Mauro Gemmi, Sergio Brovelli, Ivan Infante, Sara Bals or Liberato Manna.

Peer review information *Nature Communications* thanks Rajesh Sardar and the other, anonymous, reviewer(s) for their contribution to the peer review of this work.

Reprints and permission information is available at http://www.nature.com/reprints

Publisher's note Springer Nature remains neutral with regard to jurisdictional claims in published maps and institutional affiliations.